# Lyapunov Time for 2D Lagrangian Visualization

Filip Sadlo

**Abstract** Many concepts in computational flow visualization operate in the Lagrangian frame—they involve the integration of trajectories. A problem inherent to these approaches is the choice of an appropriate time length for the integration of these curves. While for some applications the choice of such a finite time length is straightforward, it represents in most other applications a parameter that needs to be explored and well-chosen. This becomes even more difficult in situations where different regions of the vector field require different time scopes. In this chapter, we introduce Lyapunov time for this purpose. Lyapunov time, originally defined for predictability purposes, represents the time over which a trajectory is predictable, i.e., not dominated by error. We employ this concept for steering the integration time in direct visualization by trajectories, and for derived representations such as line integral convolution and delocalized quantities. This not only provides significant visualizations related to time-dependent vector field topology, but at the same time incorporates uncertainty into trajectory-based visualization.

## 1 Introduction

Vector fields play an important role in various domains, and appropriate understanding is essential in many respects. While in the early years scientific visualization tended to employ the Eulerian view, e.g., using color coding or arrow glyphs for local quantities, it is nowadays increasingly the Lagrangian view based on trajectories that is employed for visualization of vector fields. This is in particular the case for time-dependent vector fields, where the straightforward Eulerian view would necessitate time-dependent visualizations, while concepts based on time-dependent trajectories, i.e., pathlines, in these fields are able to provide a notion of their true dynamics in a static picture.

Filip Sadlo
University of Stuttgart, Stuttgart, Germany, e-mail: sadlo@visus.uni-stuttgart.de

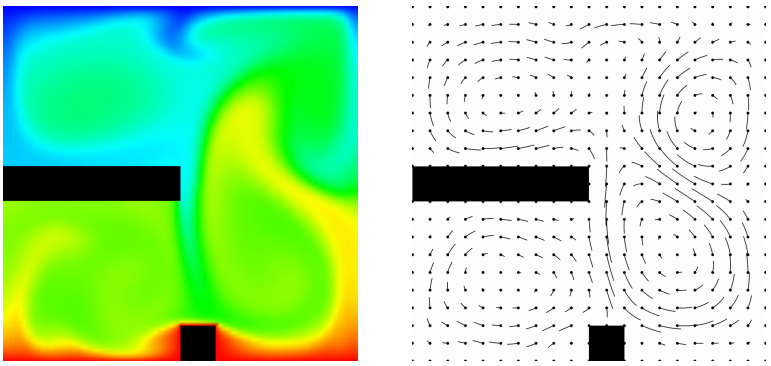

(a) (b)

**Fig. 1** Buoyant Flow dataset. The time-dependent 2D air flow is driven by a heated boundary at the bottom and a cooled boundary at the top, while gravity is pointing downward. (a) Temperature distribution at time $t_0 = 50.5008$ s, with blue at 278.15 K and red at 348.15 K. (b) Velocity field at the same time step visualized with streamlines of length 0.04 s (seeds by black dots).

Visualization techniques based on integral curves can be categorized into two main fields: dense and sparse. While dense visualizations basically represent the vector field at each point of its domain, e.g., by drawing a dense set of instantaneous trajectories (i.e., streamlines), sparse techniques, on the other hand, typically focus on salient features, e.g., they try to draw only the most important streamlines. Prominent examples of the two extremes are line integral convolution [5] (LIC) (Fig. 2), where a dense texture is obtained by smearing noise along trajectories, and vector field topology [13, 14] (Fig. 3), where isolated zeros (i.e., critical points) with saddle-type behavior of the vector field are extracted and streamlines (i.e., separatrices) are computed from these points forward and reverse, providing the essential structure of a vector field by separating its regions of qualitatively different behavior.

These two concepts, dense and sparse visualization, are typically applied separately, but cases where both are combined in an additive manner are not uncommon, since both complement each other well. While, for example, vector field topology provides a notion of the overall transport due to the vector field, LIC provides detailed morphological information about this dynamics and is therefore often used to augment topology-based visualization (Fig. 3).

Traditional vector field topology is defined in terms of asymptotic behavior of streamlines as time goes to $\pm\infty$, i.e., in practice the separatrices are integrated until they converge sufficiently close to other critical points, periodic orbits (closed streamlines), or reach the domain boundary. This raises several issues, in particular with respect to appropriateness and visual clutter. Separatrices can grow arbitrarily far from the seeding saddle point, with the result that the phenomenon of interest (the saddle-type flow behavior at the saddle point which causes the respective separatrices) has only a very remote connection to that part of the separatrix. If it makes sense to visualize and investigate such long separatrices typically depends on the application. However, such long streamlines suffer from error accumulation during

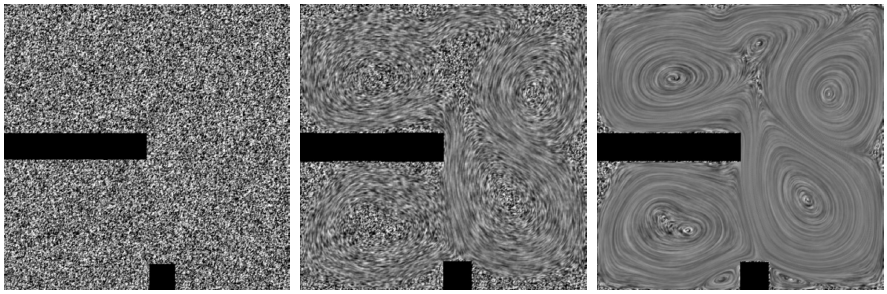

(a) (b) (c)

**Fig. 2** Line integral convolution in Buoyant Flow dataset at $t_0 = 50.5008$ s, based on streamlines in original field (no normalization of velocity). No advection LIC (a) reveals noise texture, advection with $T = \pm 0.01$ s (b) indicates flow, while advection time $T = \pm 0.1$ s (c) reveals its features.

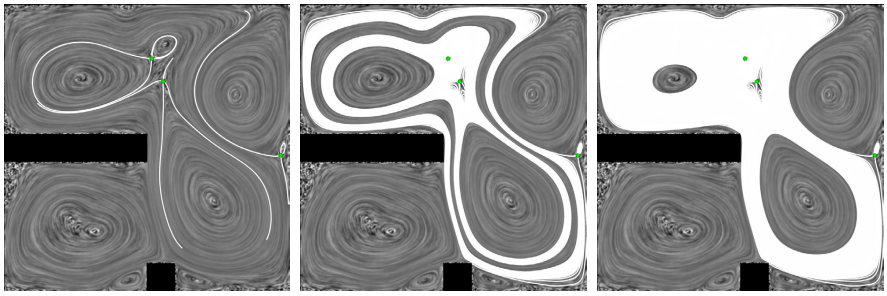

(a) (b) (c)

**Fig. 3** Traditional vector field topology extracting saddle-type critical points (green) and integrating separatrices (white) therefrom in forward and reverse direction. LIC with $T = \pm 0.1$ s provides context. (a) Separatrices of integration length 2.0 s indicate qualitatively different regions of the vector field. (b) Increasing integration of separatrix streamlines to 100.0 s can clutter visualization (in this case due to non-vanishing divergence), in particular if integration time is further increased (1000.0 s) (c). Besides insignificant visualization, this can cause prohibitive computational cost.

integration, and visual clutter during inspection. Visual clutter can in particular impede proper analysis if the vector field exhibits vortical flow that is not divergence-free. The example shown in Fig. 3(c) does, due to constraints in computation time, not show the full-size separatrices, which would fill the complete vortical structure, resulting in insignificant visualization. Hence, limiting the length of separatrices can make sense both with respect to error accumulation and perception.

A further drawback of traditional topology-based visualization of vector fields is that it takes an instantaneous view on the field because it is based on streamlines. Thus, in the case of time-dependent vector field data, it would need to be applied to isolated time steps, which cannot provide appropriate insight into the true time-dependent dynamics. During the last decade, the finite-time Lyapunov exponent [11] (FTLE) field proved successful in providing a basis for topology-based visualization of time-dependent vector fields. As will be detailed in Sec. 3, the FTLE measures the divergence of pathlines with finite time length and is therefore able to indicate

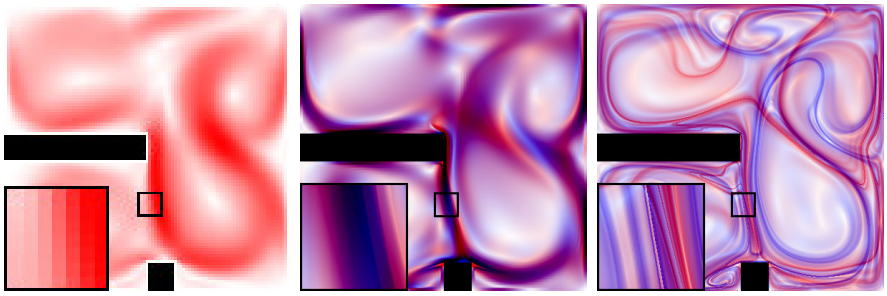

(a) (b) (c)

**Fig. 4** Pathline-based FTLE in Buoyant Flow dataset, with $t_0 = 50.5008$ s, forward (red) and reverse (blue), with zoomed-in region (black box). Resolution of FTLE features is independent of original vector field data. (a) Velocity magnitude reflects resolution of original data. (b) FTLE with advection time $T = \pm 0.1$ s exhibits features that require higher resolution, and FTLE with advection time $T = \pm 1.0$ s (c) requires even higher resolution.

the boundaries between regions of qualitatively different time-dependent transport behavior. As a consequence, computation of the FTLE field requires to start a pathline at each sample point (and time step of the FTLE field), turning this concept into a large-scale problem, even for vector fields with very low resolution. The rationale behind this is that due to its Lagrangian nature, the FTLE does not reflect the local properties of a vector field. Since each pathline traverses a substantial part of the vector field, the FTLE typically exhibits highly complex structures, far beyond the variation of, e.g., tensor-product linear interpolation of the vector field itself (Fig. 4). In fact, its detail, including the length and sharpness of its ridges, grows with increasing finite advection time $T$ (Fig. 5). The high computational cost led to various acceleration techniques, e.g., related to adaptive mesh refinement [8, 26] and using distributed compute environments [20].

So far, Lagrangian visualization techniques, such as the FTLE or LIC, typically employ uniform integration time, i.e., all underlying integral curves are of equal integration length. Depending if the vector field is normalized or not, this leads to constant-length or constant-time integral curves, respectively. In time-dependent fields, where such a normalization is not directly applicable, the integration time has to be adjusted to the phenomenon under investigation. While finding a global integration time that fits the overall visualization goal might be possible in some cases, it is rather common that a vector field exhibits different spatial and temporal scales, which necessitate different finite time intervals for Lagrangian analysis. This difficulty was the motivation for the finite-size Lyapunov exponent (FSLE) introduced by Aurell et al. [2]. Instead of prescribing the integration time and measuring the divergence of the endpoints of the trajectories, as in the case of the FTLE, the FSLE prescribes a separation factor and measures how long it takes for particles (trajectories) to separate by this factor. Hence, the FSLE can be seen as the dual for the FTLE. In other words, instead of prescribing a time scale for the analysis, as in the case of the FTLE, the FSLE employs a spatial scale by varying the time scale.

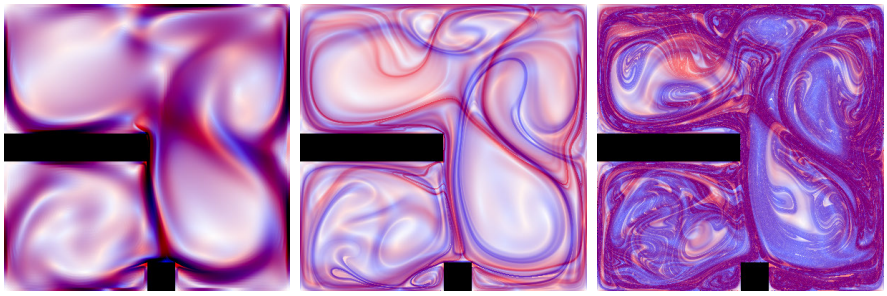

(a) (b) (c)

**Fig. 5** Pathline-based FTLE with $t_0 = 50.5008$ s, forward (red) and reverse (blue). Increasing advection time $T$ increases length of its ridges, $T = \pm 0.1$ s (a), $T = \pm 1.0$ s (b), and $T = \pm 5.0$ s (c). Insufficient advection time results fuzzy features which do not reflect the topology of the vector field (a). Too high advection time makes it very difficult to sample the features due to aliasing (c).

In this chapter, we employ Lyapunov time (LT) for the visualization of 2D time-dependent vector fields to address the aforementioned issues. Lyapunov time reflects the limits of predictability of a system, i.e., it relates to the duration over which trajectories are not dominated by error accumulation. Hence, we propose to utilize LT for steering the integration duration in trajectory-based visualization. Due to its close relation to the FTLE and FSLE, the resulting visualizations are related to time-dependent vector field topology. In Sec. 2, we give an overview of less closely related work, followed by a more formal introduction to the FTLE, FSLE, and LT concepts in Sec. 3. In Sec. 4, we present the results of LT-guided visualization, and in Sec. 5 we draw conclusions and discuss possible future work.

## 2 Related Work

Most closely related works in the field of dense Lagrangian visualization are texture advection techniques such as line integral convolution due to Cabral and Leedom [5], and delocalization of quantities due to Fuchs et al. [7], where quantities such as temperature or vortex indicators are averaged along pathlines.

Traditional (streamline-based) vector field topology was established in visualization by the works due to Perry and Chong [23], Helman and Hesselink for 2D [13] and 3D [14] flow, and Globus et al. [9]. Later works include those by Hauser et al. [18] and Theisel et al. [33], the former in the field of dynamical systems, and the latter regarding the visualization of homoclinic (heteroclinic) orbits, i.e., streamlines that connect the same (different) saddle point in 3D. Beyond that, the vector field topology concept was utilized in a variety of visualization techniques, e.g., for achieving significant streamline placement [38] or guiding streamsurface-based visualization in recirculating flow [21]. Other works in the context of recirculating flow include the visualization of the magnetic field in fusion reactors [30] and recir-

culation in general [22]. More recently, Bachthaler et al. [4] derived a vector field topology concept for the visualization of magnetic flux in 2D fields.

In the field of time-dependent vector field topology, Haller proposed [11] and Shadden et al. defined [32] Lagrangian coherent structures (LCS), the counterpart to separatrices in time-dependent fields, to be ridges in the FTLE field. A good introduction to the topic is the tutorial due to Shadden [31] and the survey by Pobitzer et al. [24]. Sadlo and Peikert [27] proposed to extract LCS using the height ridge concept due to Eberly [6]. Shadden et al. [32] and later Sadlo et al. [28] investigate the choice of the uniform finite time scope for FTLE computation, while Kasten et al. [17] proposed a local computation, and Üffinger et al. [37] examined the linearization involved in traditional FTLE computation and proposed alternatives beyond first-order approximation. While the majority of research focuses on the geometric shape of LCS, Bachthaler et al. [3] presented a visualization technique for the dynamics within LCS in 2D fields, i.e., for the stretching and squeezing in tangential direction. Beyond that, the LCS concept was also extended to tensor fields [35, 15] and transport in advection-diffusion flow [25], and used for computational steering of flow simulations [1]. Recent advances in time-dependent vector field topology include the reinterpretation of LCS as streakline-based vector field topology in 2D [29] and 3D [36] vector fields. Based on the findings of Haller [10], Ide et al. [16], and Mancho et al. [19], Sadlo et al. reinterpreted hyperbolic trajectories [10] as degenerate streaklines with hyperbolic behavior and their manifolds (LCS) as streak manifolds converging forward or reverse to these degenerate streaklines within finite time intervals. In contrast to traditional LCS extraction based on FTLE ridges, streak-based LCS avoid false positives caused by shear flow (similar to [12]), provide high-quality results, and are of lower computational cost, however, with the drawback that the degenerate streaklines (hyperbolic trajectories) have to be determined at high accuracy.

None of these techniques employ varying integration time for sets of trajectories and neither do they involve predictability considerations in this respect, in contrast to the approach based on Lyapunov time we propose.

## 3 FTLE, FSLE, and Lyapunov Time

As introduced above, the FTLE $\sigma_{t_0}^T(\mathbf{x})$ measures Lagrangian separation by determining the growth of the distance between particles during their advection over a finite advection time $T$. Haller [11] proposed to determine the FTLE by means of the flow map $\boldsymbol{\phi}_{t_0}^T(\mathbf{x})$, which maps the seed points $\mathbf{x}$ of pathlines started at time $t_0$ to their endpoints after advection for time $T$. Based on this, the FTLE can be obtained using the spectral norm $\|\cdot\|_2$ as

$$\sigma_{t_0}^T = \frac{1}{|T|} \ln \|\nabla \boldsymbol{\phi}_{t_0}^T\|_2 = \frac{1}{|T|} \ln \sqrt{\lambda_{\max}\left( (\nabla \boldsymbol{\phi}_{t_0}^T)^\top \nabla \boldsymbol{\phi}_{t_0}^T \right)}\,, \tag{1}$$

with $\lambda_{\max}(\cdot)$ representing the major eigenvalue. It can be readily seen that the FTLE basically measures the gradient of the flow map, i.e., a linearization of the largest separation of pathline endpoints with uniform advection time $T$.

The FSLE can be seen as a dual approach: here, the separation factor $s$ is prescribed and the time $T_s$ is measured, until this factor is achieved. As proposed by Sadlo and Peikert [26], the FSLE $\hat{\sigma}^s_{t_0}(\mathbf{x})$ can be also computed from the flow map, using the FTLE as follows:

$$\hat{\sigma}^s_{t_0} = \frac{1}{|T^s_{t_0}|} \ln s \,, \tag{2}$$

with

$$T^s_{t_0} = \arg\min_{|T|} \|\nabla \boldsymbol{\phi}^T_{t_0}\|_2 \stackrel{!}{=} s \,. \tag{3}$$

For efficient computation [26], the flow map $\boldsymbol{\phi}^T_{t_0}(\mathbf{x})$ can be computed incrementally for increasing $T$ until Eqn. 3 is satisfied.

The Lyapunov time $\tau^e_{t_0}(\mathbf{x})$ represents the smallest time interval that is necessary for a perturbation started at $\mathbf{x}$ and time $t_0$ to grow by a factor of Euler's number $e$,

$$\tau^e_{t_0} = \arg\min_{|T|} \|\nabla \boldsymbol{\phi}^T_{t_0}\|_2 \stackrel{!}{=} e \,. \tag{4}$$

Hence, using Eqn. 2, LT relates to the FSLE as follows:

$$\tau^e_{t_0} = \frac{1}{\hat{\sigma}^e_{t_0}} \ln e = \frac{1}{\hat{\sigma}^e_{t_0}} \,. \tag{5}$$

Throughout this chapter, we compute LT according to Eq. 5, using the algorithm [26] for FSLE computation. Due to its high computational complexity, the cost for LT computation typically predominates that of the subsequent LT-constrained trajectory-based visualization (Sec. 4).

It is of course possible to compute the FTLE, FSLE, and LT for stationary vector fields, or for isolated time steps of time-dependent fields, using streamlines. It has to be noted, however, that the resulting structures cannot be consistent with traditional vector field topology in general, although they may be similar sometimes [34, 27], because, while the FTLE, FSLE, and LT are Galilean-invariant, traditional vector field topology is not. This is demonstrated in Fig. 6.

## 4 Lyapunov Time for Visualization

The utility of constraining integration time with LT in trajectory-based visualization is demonstrated with three applications using the Buoyant Flow dataset (Fig. 1). First, we include LT in sparse trajectory-based visualization (Sec. 4.1). Then we exemplify LT-based visualization by means of LIC (Sec. 4.2). Finally, we provide results for LT-constrained delocalization of quantities (Sec. 4.3).

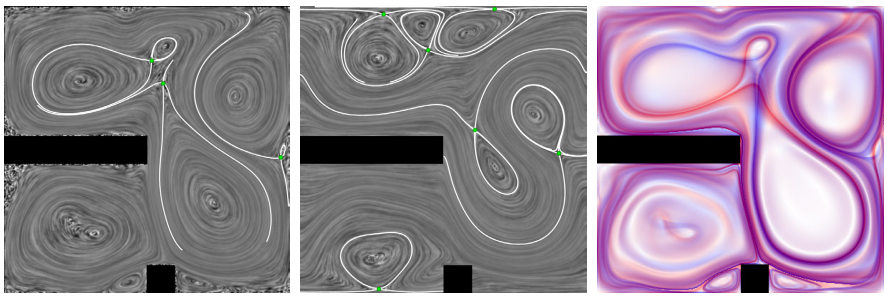

(a) (b) (c)

**Fig. 6** Galilean invariance of FTLE in Buoyant Flow dataset at $t_0 = 50.5008$ s. Traditional vector field topology is not Galilean-invariant, i.e., result from original frame of reference (a) (Fig. 3(a)) differs from result if observer moves from right to left at speed 0.05 m/s (b). (c) Streamline-based FTLE with $T = 1$ s, forward (red) and reverse (blue), is identical in both frames and exhibits, in this example, features similar, but not identical, to (a).

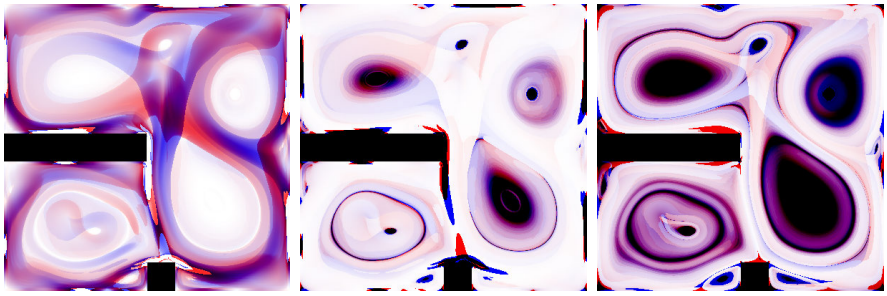

(a) (b) (c)

**Fig. 7** (a) FSLE $\hat{\sigma}^{e}_{50.5008}$ forward (red) and reverse (blue). (b) LT $\tau^{e}_{50.5008}$ computed from (a), forward (red) and reverse (blue). (c) "Lyapunov time" $\tau^{10}_{50.5008}$ with scaling factor 10 for comparison.

Since LIC requires streamlines for its generation and to support comparability and interpretability, we use streamlines for generating all results in this section, i.e., the FTLE, FSLE, and LT as well the derived trajectories and delocalizations are based on streamlines. In practice, however, our approach does address both steady and time-dependent vector fields. Our results are based on the fields shown in Fig. 7. Figure 7(a) shows the streamline-based FSLE with separation factor $e$ and Fig. 7(b) the LT $\tau^{e}_{50.5008}$ derived therefrom. Since $\tau^{e}_{50.5008}$ is rather restrictive, we also provide results for $\tau^{10}_{50.5008}$, the "Lyapunov time" with separation factor 10 (Fig. 7(c)).

## *4.1 Sparse LT Trajectories*

Motivated by the difficulties demonstrated in Fig. 3, we first employ LT for limiting the integration length of separatrices (Fig. 8). Since the goal of vector field topol-

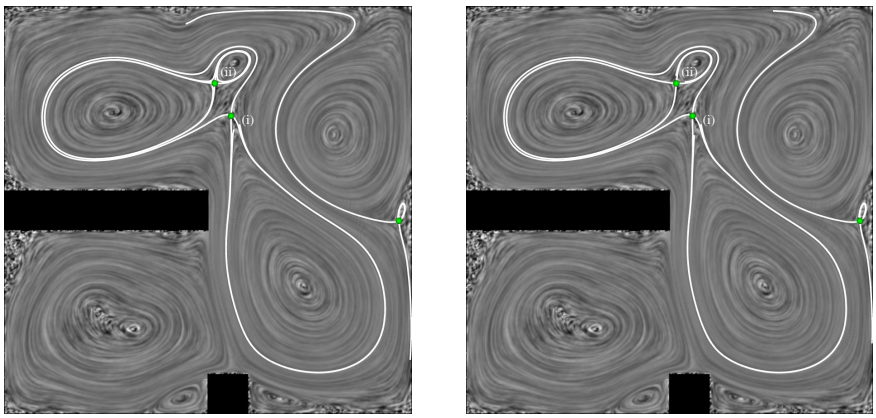


(a) (b)

**Fig. 8** (a) Visualization by separatrices with uniform integration length of 3 s. While the separatrices just reach the originating saddle point at (i), they pass it at (ii), resulting in insignificant visualization there. (b) Visualization by separatrices constrained to $8.0 \cdot \tau^{e}_{50.5008}$. Separatrices reach saddle point both at (i) and (ii), providing a more concise and better comprehensible visualization. Confer Fig. 3(a) for uniform integration length of 2 s, where separatrices reach (ii) but not (i).

ogy is to depict the regions of qualitatively different behavior and since divergence is comparably small in the examined data, we aim at separatrices that perform a "single turn", i.e., that reach the critical point where they were seeded. This way they indicate the substantial regions and at the same time the effects of divergence. While a global selection of integration time cannot achieve this goal (see Figs. 3(a) and 8(a)), constraining integration by $8.0 \cdot \tau^{e}_{50.5008}$ achieves this goal for the saddles at (i) and (ii) (Fig. 8(b))—providing a significant visualization of the dynamics.

Next, we limit integration time with LT for regularly seeded streamlines (Fig. 9). Figures 9(a) and 9(d) show uniform integration in forward and reverse direction, respectively. Note that in our current approach, we do not employ streamline placement to achieve an even placement of the lines—instead we use rather short integration times to prevent excessive visual clutter. We want to address streamline placement that involves LT as future work. Limiting integration length with LT not only incorporates predictability aspects, it provides at the same time structures that reflect the coherent structures. We found that limiting integration time with $\tau^{e}_{50.5008}$ (Figs. 9(b) and 9(e)) was rather restrictive, we preferred using $\tau^{10}_{50.5008}$ (Figs. 9(c) and 9(f)), as these provided more pronounced structures. As illustrated in Figs. 9(g) and 9(h), our approach reveals the regions of qualitatively different behavior.

## *4.2 LT LIC*

The results from regularly seeded streamlines from Sec. 4.1 directly motivate limiting integration in LIC using LT (Fig. 10). Again, $\tau^{10}_{50.5008}$, in particular $0.01 \cdot \tau^{10}_{50.5008}$

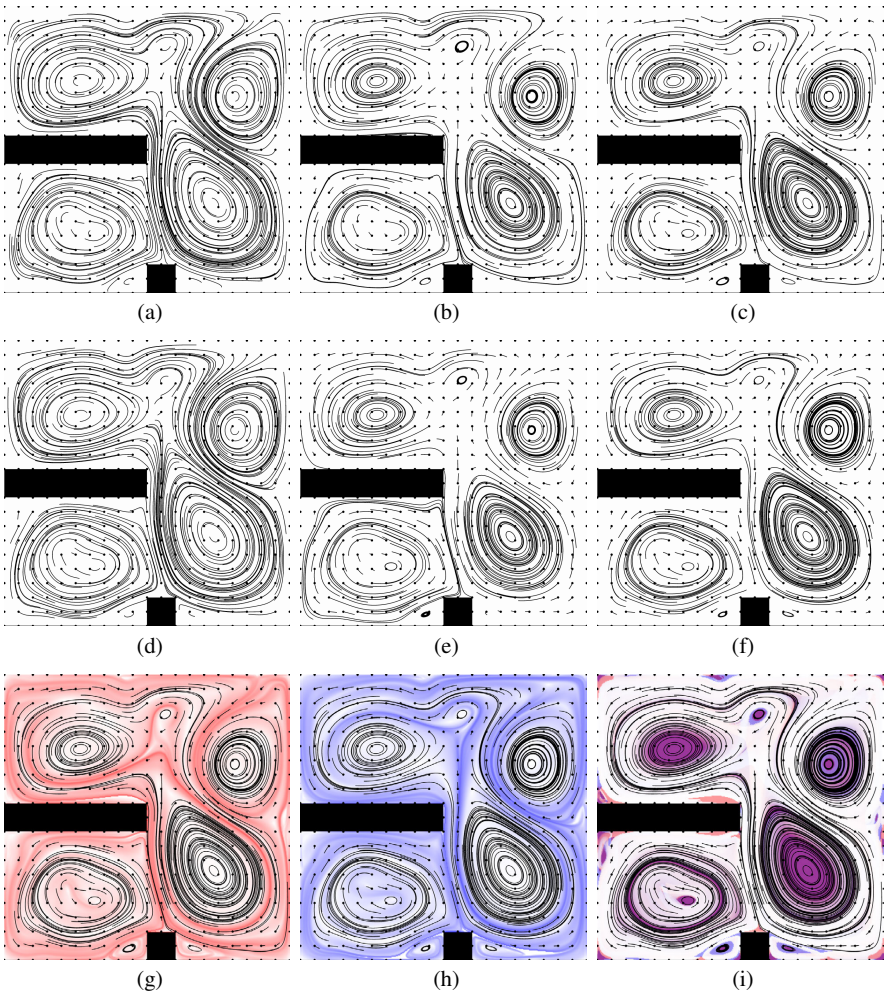


**Fig. 9** (a)–(c) Forward streamlines at $t_0 = 50.5008$ s, of length 0.4 s (a), $0.3 \cdot \tau^e_{50.5008}$ (b), and $0.1 \cdot \tau^{10}_{50.5008}$ (c). (d)–(f) Same for reverse streamlines. It is apparent that $0.1 \cdot \tau^{10}_{50.5008}$ provides more expressive results. (g) Comparison of (c) with forward FTLE from Fig. 6(c) shows that coherent regions are well represented. (h) Same for (f) with reverse FTLE. (i) Forward (c) and reverse (f) streamlines together with forward (red) and reverse (blue) $0.1 \cdot \tau^{10}_{50.5008}$ for context.

(Fig. 10(f)), leads to results that depict coherent regions in a more pronounced manner. In LT LIC visualizations, chaotic (less predictable) regions can be identified by more noisy areas whereas predictable regions are represented with more line-like structures. Compared to LT trajectories (Sec. 4.1), LT LIC provides a more continuous and more detailed picture of predictability and coherence.

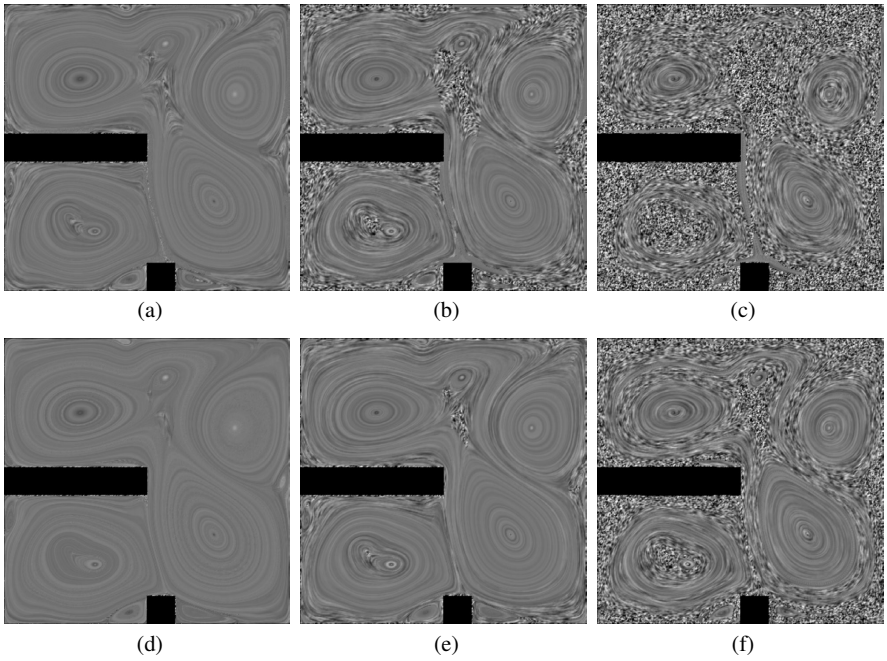

**Fig. 10** Limiting LIC with forward and reverse $\tau^{e}_{50.5008}$, using $1.0 \cdot \tau^{e}_{50.5008}$ (a), $0.1 \cdot \tau^{e}_{50.5008}$ (b), and $0.01 \cdot \tau^{e}_{50.5008}$ (c) shows coherent regions. However, using forward and reverse $\tau^{10}_{50.5008}$, using $1.0 \cdot \tau^{10}_{50.5008}$ (d), $0.1 \cdot \tau^{10}_{50.5008}$ (e), and $0.01 \cdot \tau^{10}_{50.5008}$ (f) provides more significant results.

## *4.3 LT Delocalization*

In our final example, we employ LT for the delocalization [7] of scalar quantities. The concept of delocalization was originally used to make vortex indicators more coherent. For each sample point, a trajectory is seeded there, a scalar field, in our case temperature, is averaged along the trajectory, and the result is stored at the seed point of the trajectory. Hence, delocalization can be interpreted as Lagrangian averaging of quantities (Fig. 10).

In contrast to the original approach (Figs. 11(a)–(e)), which uses uniform integration length, we limit the trajectories by LT (Figs. 11(g)–(i)). While the temperature field from the simulation is subject to excessive diffusion (Fig. 11(c)) due to numerical diffusion in the solver, delocalization provides a tool for investigating the advection of quantities with reduced diffusion, in particular the delocalization in direction reverse to the flow. Compared to traditional delocalization, LT delocalization takes at the same time into account predictability of the involved trajectories, which limits the resulting structures but prevents misinterpretation with respect to accumulation of integration error. Nevertheless, we find it more difficult to interpret the overall results from LT delocalization—providing a visualization of the underlying LT trajectories for context is important.

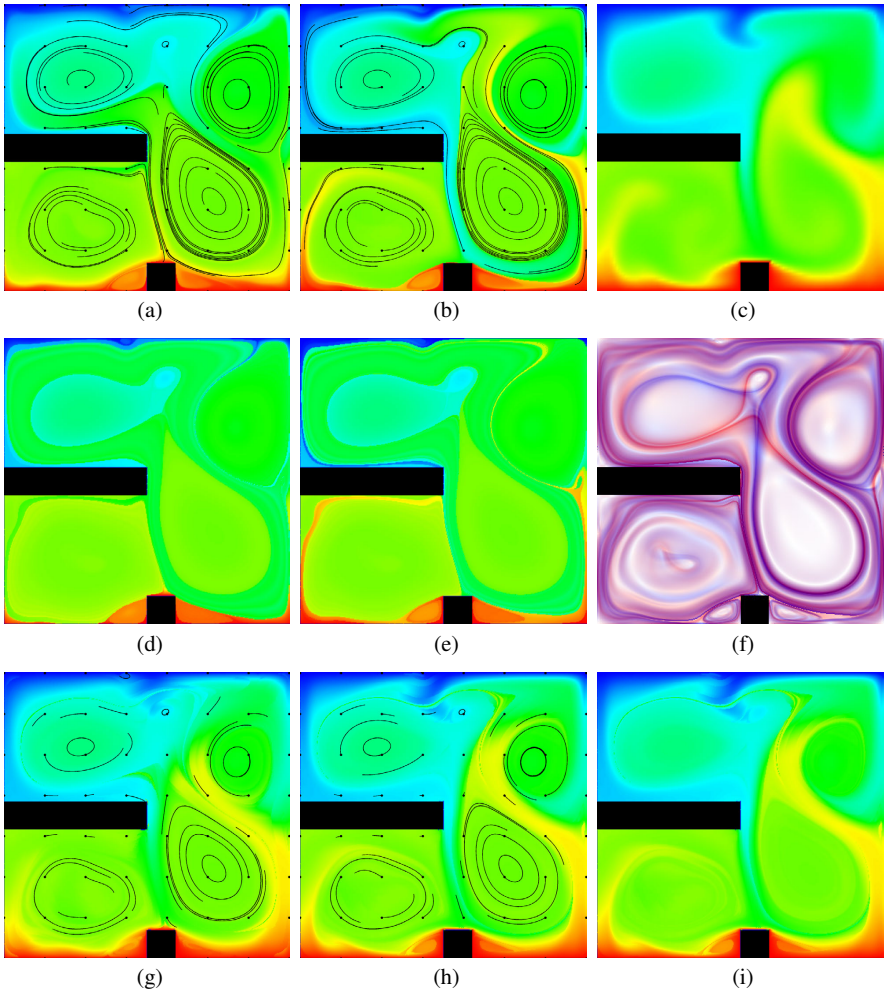

**Fig. 11** Delocalization of temperature (c) (blue at 278.18 K, red at 348.18 K) at $t_0 = 50.5008$ s, using streamlines of length 1.0 s forward (a) and reverse (b), with selected streamlines. Delocalization with length 10.0 s forward (d) and reverse (e) reveals coherent structures (compare streamline-based FTLE (f), same as Fig. 6(c)). Limiting delocalization time with $1.0 \cdot \tau^{10}_{50.5008}$ forward (g) and reverse (h),(i) does not provide coherent structures as clearly, but shows predictability, i.e., only predictable structures with respect to temperature advection are shown.

## 5 Conclusion

We introduced Lyapunov time in trajectory-based visualization and demonstrated its use for separatrices and direct visualization by sets of trajectories, for LIC, and for the delocalization of quantities. The resulting visualizations not only reflect predictability limitations in these concepts, they reveal at the same time the topological

structure of the vector fields due to the close relation between Lyapunov time and the FSLE field. As future work inspired from our results in Sec. 4.1, we plan to develop streamline placement strategies that take into account Lyapunov time, both for predictability purposes and topological expressiveness.

**Acknowledgements** The author would like to thank the German Research Foundation (DFG) for financial support within the *Cluster of Excellence in Simulation Technology* (EXC 310).

## References

1. M. Ament, S. Frey, F. Sadlo, T. Ertl, and D. Weiskopf. GPU-based two-dimensional flow simulation steering using coherent structures. In *Proceedings of Second International Conference on Parallel, Distributed, Grid and Cloud Computing for Engineering*.
2. E. Aurell, G. Boffetta, A. Crisanti, G. Paladin, and A. Vulpiani. Predictability in the large: an extension of the concept of Lyapunov exponent. *J. Phys. A*, 30:1–26, 1997.
3. S. Bachthaler, F. Sadlo, C. Dachsbacher, and D. Weiskopf. Space-time visualization of dynamics in Lagrangian coherent structures of time-dependent 2D vector fields. In *Proceedings of International Conference on Information Visualization Theory and Applications*, pages 573–583, 2012.
4. S. Bachthaler, F. Sadlo, R. Weeber, S. Kantorovich, C. Holm, and D. Weiskopf. Magnetic flux topology of 2D point dipoles. *Comput. Graph. Forum*, 31(3):955–964, 2012.
5. B. Cabral and L. C. Leedom. Imaging vector fields using line integral convolution. In *Proceedings of 20th Annual Conference on Computer Graphics and Interactive Techniques*, SIGGRAPH '93, pages 263–270. ACM, 1993.
6. D. Eberly. *Ridges in Image and Data Analysis. Computational Imaging and Vision.* Kluwer Academic Publishers, 1996.
7. R. Fuchs, R. Peikert, F. Sadlo, B. Alsallakh, and M. E. Gröller. Delocalized unsteady vortex region detectors. In *Proceedings of International Workshop on Vision, Modeling and Visualization*, pages 81–90, 2008.
8. C. Garth, F. Gerhardt, X. Tricoche, and H. Hagen. Efficient computation and visualization of coherent structures in fluid flow applications. *IEEE Trans. Vis. Comput. Graphics*, 13(6):1464–71, 2007.
9. A. Globus, C. Levit, and T. Lasinski. A tool for visualizing the topology of three-dimensional vector fields. In *Proceedings of IEEE Visualization*, pages 33–40, 408, 1991.
10. G. Haller. Finding finite-time invariant manifolds in two-dimensional velocity fields. *Chaos*, 10(1):99–108, 2000.
11. G. Haller. Distinguished material surfaces and coherent structures in three-dimensional fluid flows. *Phys. D*, 149(4):248–277, 2001.
12. G. Haller. A variational theory of hyperbolic Lagrangian coherent structures. *Phys. D*, 240(7):574–598, 2011.
13. J. Helman and L. Hesselink. Representation and display of vector field topology in fluid flow data sets. *IEEE Computer*, 22(8):27–36, 1989.
14. J. Helman and L. Hesselink. Visualizing vector field topology in fluid flows. *IEEE Computer Graphics and Applications*, 11(3):36–46, 1991.
15. M. Hlawatsch, J. Vollrath, F. Sadlo, and D. Weiskopf. Coherent structures of characteristic curves in symmetric second order tensor fields. *IEEE Trans. Vis. Comput. Graphics*, 17(6):781–794, 2011.
16. K. Ide, D. Small, and S. Wiggins. Distinguished hyperbolic trajectories in time-dependent fluid flows: analytical and computational approach for velocity fields defined as data sets. *Nonlinear Processes in Geophysics*, 9(3/4):237–263, 2002.

17. J. Kasten, C. Petz, I. Hotz, B. Noack, and H.-C. Hege. Localized finite-time Lyapunov exponent for unsteady flow analysis. In *Proceedings of International Workshop on Vision, Modeling and Visualization*, pages 265–274, 2009.
18. H. Löffelmann, H. Doleisch, and E. Gröller. Visualizing dynamical systems near critical points. In *Proceedings of Spring Conference on Computer Graphics and its Applications*, pages 175–184, 1998.
19. A. M. Mancho, D. Small, S. Wiggins, and K. Ide. Computation of stable and unstable manifolds of hyperbolic trajectories in two-dimensional, aperiodically time-dependent vector fields. *Phys. D*, 182:188–222, 2003.
20. A. Panagiotidis, D. Kauker, F. Sadlo, and T. Ertl. Distributed computation and large-scale visualization in heterogeneous compute environments. In *Proceedings of 11th International Symposium on Parallel and Distributed Computing*, pages 87–94, 2012.
21. R. Peikert and F. Sadlo. Topology-guided visualization of constrained vector fields. In *Topology-Based Methods in Visualization*, pages 21–34. Springer, 2007.
22. R. Peikert and F. Sadlo. Visualization methods for vortex rings and vortex breakdown bubbles. In *Proceedings of EuroVis*, pages 211–218, 2007.
23. A. E. Perry and M. S. Chong. A description of eddying motions and flow patterns using critical-point concepts. *Annual Review of Fluid Mechanics*, 19:125–155, 1987.
24. A. Pobitzer, R. Peikert, R. Fuchs, B. Schindler, A. Kuhn, H. Theisel, K. Matkovic, and H. Hauser. The state of the art in topology-based visualization of unsteady flow. *Comput. Graph. Forum*, 30(6):1789–1811, 2011.
25. F. Sadlo, G. K. Karch, and T. Ertl. Topological features in time-dependent advection-diffusion flow. In *Topological Methods in Data Analysis and Visualization III*, pages 217–231. Springer, 2014.
26. F. Sadlo and R. Peikert. Efficient visualization of Lagrangian coherent structures by filtered AMR ridge extraction. *IEEE Trans. Vis. Comput. Graphics*, 13(6):1456–1463, 2007.
27. F. Sadlo and R. Peikert. Visualizing Lagrangian coherent structures and comparison to vector field topology. In *Topology-Based Methods in Visualization II*, pages 15–30. Springer, 2009.
28. F. Sadlo, M. Üffinger, T. Ertl, and D. Weiskopf. On the finite-time scope for computing Lagrangian coherent structures from Lyapunov exponents. In *Topological Methods in Data Analysis and Visualization II*, pages 269–281. Springer, 2012.
29. F. Sadlo and D. Weiskopf. Time-dependent 2-D vector field topology: An approach inspired by Lagrangian coherent structures. *Comput. Graph. Forum*, 29(1):88–100, 2010.
30. A. Sanderson, G. Chen, X. Tricoche, D. Pugmire, S. Kruger, and J. Breslau. Analysis of recurrent patterns in toroidal magnetic fields. *IEEE Trans. Vis. Comput. Graphics*, 16(6):1431–1440, 2010.
31. S. Shadden. LCS tutorial. http://mmae.iit.edu/shadden/LCS-tutorial/contents.html.
32. S. C. Shadden, F. Lekien, and J. E. Marsden. Definition and properties of Lagrangian coherent structures from finite-time Lyapunov exponents in two-dimensional aperiodic flows. *Phys. D*, 212:271–304, 2005.
33. H. Theisel, T. Weinkauf, H.-C. Hege, and H.-P. Seidel. Saddle connectors - an approach to visualizing the topological skeleton of complex 3D vector fields. In *Proceedings of IEEE Visualization*, pages 225–232, 2003.
34. X. Tricoche, C. Garth, A. Sanderson, and K. Joy. Visualizing invariant manifolds in area-preserving maps. In *Topological Methods in Data Analysis and Visualization II*, pages 109–124. Springer, 2012.
35. X. Tricoche, M. Hlawitschka, S. Barakat, and C. Garth. Beyond topology: A Lagrangian metaphor to visualize the structure of 3D tensor fields. *New Developments in the Visualization and Processing of Tensor Fields*, 2012.
36. M. Üffinger, F. Sadlo, and T. Ertl. A time-dependent vector field topology based on streak surfaces. *IEEE Trans. Vis. Comput. Graphics*, 19(3):379–392, 2013.
37. M. Üffinger, F. Sadlo, M. Kirby, C. Hansen, and T. Ertl. FTLE computation beyond first-order approximation. In *Short Paper Proceedings of Eurographics*, pages 61–64, 2012.
38. K. Wu, Z. Liu, S. Zhang, and R. Moorhead. Topology-aware evenly spaced streamline placement. *IEEE Trans. Vis. Comput. Graphics*, 16(5):791–801, 2010.